

Microscopic origin of magnetism in monolayer 3d transition metal dihalides

Kira Riedl,^{1,*} Danila Amoroso,^{2,3,*} Steffen Backes,⁴ Aleksandar Razpopov,¹
Thi Phuong Thao Nguyen,^{5,6} Kunihiko Yamauchi,^{5,6} Paolo
Barone,⁷ Stephen M. Winter,⁸ Silvia Picozzi,² and Roser Valentí¹

¹*Institut für Theoretische Physik, Goethe-Universität Frankfurt, Max-von-Laue-Strasse 1, 60438 Frankfurt am Main, Germany*

²*Consiglio Nazionale delle Ricerche CNR-SPIN, c/o Università degli Studi 'G. D'Annunzio', 66100, Chieti, Italy*

³*NanoMat/Q-mat/CESAM, Université de Liège, B-4000 Liège, Belgium*

⁴*CPHT, CNRS, Ecole Polytechnique, Institut Polytechnique de Paris, Route de Saclay, 91128 Palaiseau, France, F-91128 Palaiseau, France Collège de France, 11 place Marcelin Berthelot, 75005 Paris,*

France European Theoretical Spectroscopy Facility, 91128 Palaiseau, France, Europe

⁵*Institute of Scientific and Industrial Research ISIR-SANKEN,*

Osaka University, 8-1 Mihogaoka, Ibaraki, Osaka, 567-0047, Japan

⁶*Department of Precision Engineering, Graduate School of Engineering,*

Osaka University, 2-1 Yamadaoka, Suita, Osaka 565-0871, Japan

⁷*Consiglio Nazionale delle Ricerche CNR-SPIN, Area della Ricerca di Tor Vergata, Via del Fosso del Cavaliere 100, I-00133 Rome, Italy*

⁸*Department of Physics and Center for Functional Materials, Wake Forest University, Winston-Salem, North Carolina 27109, United States*

(Dated: June 2, 2022)

Motivated by the recent wealth of exotic magnetic phases emerging in two-dimensional frustrated lattices, we investigate the origin of possible magnetism in the monolayer family of triangular lattice materials MX_2 ($M=\{V, Mn, Ni\}$, $X=\{Cl, Br, I\}$). We first show that consideration of general properties such as filling and hybridization enables to formulate trends for the most relevant magnetic interaction parameters. In particular, we observe that the effects of spin-orbit coupling (SOC) can be effectively tuned through the ligand elements as the considered 3d transition metal ions do not strongly contribute to the anisotropic component of the inter-site exchange interaction. Consequently, we find that the corresponding SOC matrix-elements differ significantly from the atomic limit. In a next step and by using two *ab initio*-based complementary approaches, we extract realistic effective spin models and find that in the case of heavy ligand elements, SOC effects manifest in anisotropic exchange and single-ion anisotropy only for specific fillings.

I. INTRODUCTION

Transition-metal-based materials with magnetically frustrated lattices have been at the center of intensive research for several decades^{1–6} due to the presence of fascinating phases ranging from unconventional ordered states to spin liquids. In recent years, two-dimensional (2D) van der Waals magnets have emerged as a new platform for exotic magnetism in reduced dimensions. One of the most prominent examples is the honeycomb spin-1/2 α -RuCl₃ which has dominant frustrating Kitaev interactions^{7–13} as a result of an interplay of crystal field splitting, Coulomb repulsion and spin-orbit coupling of Ru 4d electrons. Anisotropic exchange interactions are also being discussed in the context of 2D van der Waals magnets with 3d transition metals, such as the spin-3/2 CrI₃, where SOC effects arise from the ligand iodine mediating the exchange; nevertheless, the underlying physics and strength of such interactions still remain rather controversial^{14–21}.

Motivated by the significance of understanding the origin of mechanisms behind the different magnetic interactions in 2D van der Waals (vdW) magnets, we study here the case of magnetic exchange interactions of selected monolayer 3d transition metal dihalides MX_2 ($M=\{V, Mn, Ni\}$, $X=\{Cl, Br, I\}$), where the cations M are in the

octahedral environment of the ligand X anions, and are arranged in a triangular lattice, as depicted in Fig. 1(a). These materials exhibit a variety of interesting properties. For example, type-II multiferroicity was reported in bulk NiBr₂²², NiI₂²³ and MnI₂^{24,25}, where the onset of helimagnetic phases breaks inversion symmetry leading to spin-induced ferroelectricity. Such a multiferroic phase has been recently reported to survive down to the monolayer limit of NiI₂^{26,27}, while monolayer NiBr₂ and NiCl₂ have been proposed as half-excitonic insulators²⁸. The electronic structure of the 3d MX_2 compounds has been recently analyzed^{29,30}; however the magnetic exchange couplings and SOC-driven anisotropic contributions have not been fully addressed and require deeper investigation.

The purpose of the present work is twofold: (i) to uncover the microscopic mechanism behind the magnetic couplings in the 2D dihalides with 3d transition metals, and (ii) to benchmark two complementary *ab-initio* approaches for the estimation of magnetic couplings, the “projED”³¹ and “4-states”^{32,33} methods. The selected materials allow us to address the underlying processes behind the magnetic couplings by studying the influence of different electron filling through the metal elements M , and the effective spin-orbit coupling (SOC) through the ligand elements X , as schematically shown in Fig. 1(b). The magnetic properties of the respective

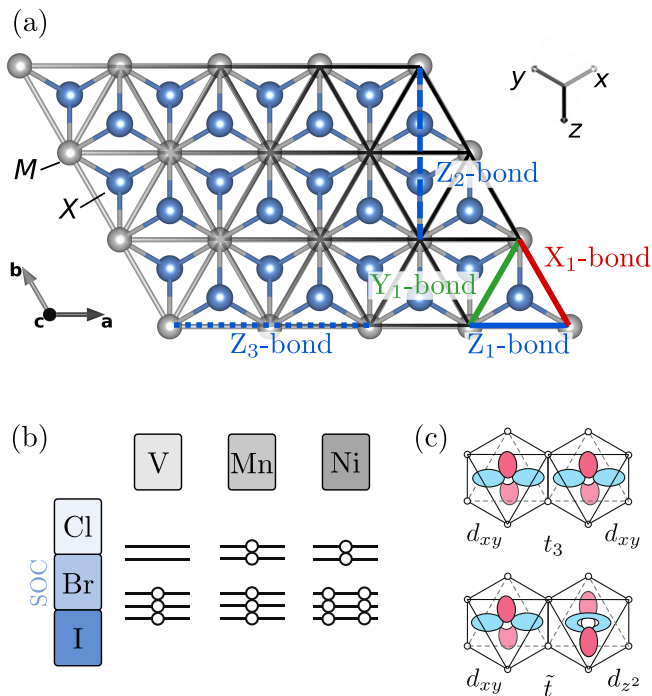


FIG. 1. (a) Common structure of the triangular MX_2 materials, for which monolayer structures are investigated in this work. Relevant bonds, the crystallographic (abc) coordinate system and the cubic (xyz) coordinate system are defined. (b) Filling for VX_2 , MnX_2 and NiX_2 with $X = \{\text{Cl}, \text{Br}, \text{I}\}$. A darker colour illustrates higher filling (grey) or stronger SOC (blue). (c) Dominant hoppings t_3 and \tilde{t} on a nearest neighbor Z_1 -bond.

materials can be then generally described in terms of effective (anisotropic) spin Hamiltonians with $S = \{3/2, 5/2, 1\}$, dependent on the filling $\{d^3, d^5, d^8\}$.

The paper is organized as follows; in Sections II and III we discuss the spin model and general trends for the magnetic exchange couplings in MX_2 considering crystal-field splittings and the Goodenough-Kanamori-Anderson rules^{34,35}. In Section IV we present our results on the *ab-initio* estimated magnetic interactions and discuss the resulting magnetic properties for the dihalide family. In Section IV we present our conclusions.

II. SPIN MODEL

The most general spin Hamiltonian model, including single-ion anisotropy \mathbb{A}_l and bilinear exchange tensors \mathbb{J}_{lm} (with sites l, m), is given by:

$$\mathcal{H} = \sum_l \mathbf{S}_l \cdot \mathbb{A}_l \cdot \mathbf{S}_l + \sum_{\langle lm \rangle} \mathbf{S}_l \cdot \mathbb{J}_{lm} \cdot \mathbf{S}_m. \quad (1)$$

For convenience, we express the single-ion anisotropy (SIA) in the crystallographic coordinate system (ab^*c), where b^* is perpendicular to the ac crystal axes, $\mathcal{H}_{\text{SIA}} =$

$A_c \sum_l (S_l^c)^2$ consistently with the symmetry of MX_2 . This allows us to easily identify the triangular layer as an easy or hard plane. On the other hand, the bond-dependent bilinear exchange parameters are most conveniently described in the cubic coordinate system (xyz), which consists of orthogonalized axes oriented approximately along $M-X$ bonds, as illustrated in Fig. 1(a). Note that the $M-X$ bonds are not perfectly orthogonal due to trigonal distortion effects.

The $P\bar{3}m1$ (space group 164) centrosymmetric monolayer structures have four independent parameters. Here, we adopt a bond-dependent parametrization corresponding to the extended Heisenberg-Kitaev model^{36,37}. In this framework, each bond is labelled after the cubic axis perpendicular to it. For a nearest-neighbor Z_1 -bond, perpendicular to the z axis, (Fig. 1(a)), the exchange couplings are then conventionally parametrized as follows:

$$\mathbb{J}_{lm} = \begin{pmatrix} J & \Gamma & \Gamma' \\ \Gamma & J & \Gamma' \\ \Gamma' & \Gamma' & J + K \end{pmatrix}. \quad (2)$$

with the (nearest neighbor) bond-isotropic Heisenberg exchange J , the anisotropic Kitaev exchange K , and the off-diagonal symmetric exchange terms Γ and Γ' . This is the most symmetric general expression for the exchange tensor given the crystal symmetries that enforce four independent parameters. The bilinear exchange matrices for the X- and Y-bond are related to Eq. (2) by C_3 rotation about the out-of-plane axis. A correspondence to a parametrization oriented along the crystallographic axes coordinate system (ab^*c) is given in Appendix A.

III. GENERAL CONSIDERATIONS

We start by identifying general traits in hybridization patterns and fillings in $3d-MX_2$ triangular lattice compounds, with edge-sharing halogen ligand octahedra. As we discuss below, this will allow us to formulate trends for the most relevant magnetic interactions.

A. Metal-ligand hybridization

The hybridization between the metal d - and ligand p -orbitals is generally expected to increase as the electronegativity difference between the two elements decreases. This affects related electronic properties, such as the local Coulomb repulsion U_{avg} , the strength of different hopping processes and the materials' SOC matrix elements. These factors all together ultimately determine the magnetic couplings.

We quantify the hybridization in MX_2 via non spin-polarized density functional theory (DFT) calculations, through the generalized gradient approximation (GGA)³⁸ orbital-resolved density of states (DOS). In particular, the energy window dominated by $p-d$ bonding orbitals contains also a finite d character that scales with

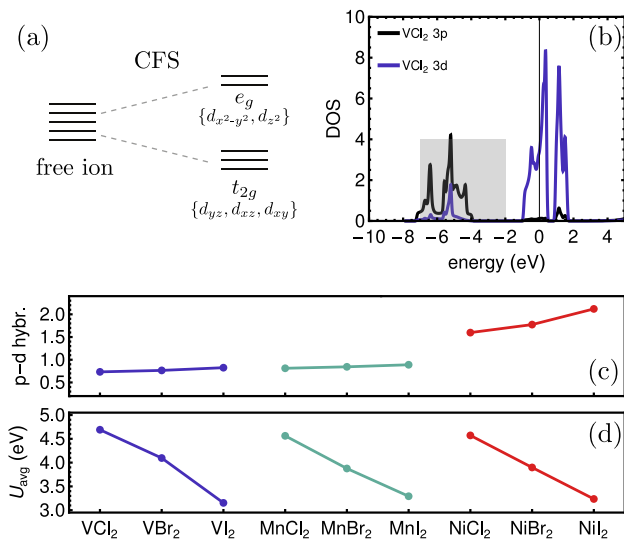


FIG. 2. (a) Cubic crystal-field splitting (CFS) of d orbitals into t_{2g} and e_g levels, (b) *ab-initio* (GGA) density of states (DOS) of VCl_2 , (c) $p-d$ hybridization, i.e. integral of $3d$ DOS in the energy region dominated by $p-d$ bonding (illustrated by the grey box in (b)), and (d) U_{avg} calculated with cRPA for each MX_2 material.

the degree of hybridization. This is illustrated for the example case of VCl_2 in Fig. 2(b), where a finite d character (in blue) is present within the relevant energy window (marked by the grey box). The integral of the metal $3d$ DOS in the respective $p-d$ bonding dominated energy window is shown for each material in Fig. 2(c). As expected, the hybridization increases with smaller electronegativity difference, i.e. for each of the considered metal elements it increases with ligand atomic number. For the NiX_2 systems, an especially strong hybridization is observed due to the larger electronegativity of nickel.

To estimate trends in the effective Coulomb interaction U_{avg} , we employed the constrained random-phase approximation (cRPA)^{39,40}, detailed in Appendix B. The results for each material are given in Table I, and U_{avg} is illustrated in Fig. 2(d). We observe a decrease of U_{avg} as a function of ligand atomic number, which can be related to the increasing metal-ligand hybridization (see Fig. 2(c)). Accordingly, we find the smallest effective interaction parameters for the strongest hybridizing, and hence most delocalized, orbitals. We have taken the cRPA values of the effective Coulomb repulsion U_{avg} and Hund’s coupling J_{avg} as input modeling parameters to estimate the magnetic interaction parameters by means of the two *ab-initio* methods (Section IV).

B. Nearest Neighbor Isotropic Exchange Interactions

In general, there are various exchange processes that are relevant to the magnetic couplings. The trends for

different ligands and filling can be rationalized by considering effective $d-d$ hopping integrals estimated via Wannier projection^{41,42} onto a d -only basis. Precise hopping parameters estimated using non-relativistic DFT calculations with the full potential local orbital (FPLO)⁴³ basis as well as complete expressions for symmetry-allowed hopping matrices are given in Appendix C. An alternative analysis, based on spin-polarized Wannier projection is detailed in Appendix D.

Over the entire series of materials, we find that the dominant nearest neighbor hoppings are t_3 and \tilde{t} ; on the Z_1 -bond, for example, these correspond to $t_{(xy;xy)}$ and $t_{(xy;z^2)}$, respectively, illustrated in Fig. 1(c). For the ideal 90° $M-X-M$ bond geometry, t_3 is mainly the result of direct overlap, while \tilde{t} has contributions from both direct hopping and ligand hybridization (with the latter dominating). Consequently, \tilde{t} becomes increasingly important as the $p-d$ hybridization increases.

The consequences of the dominant $d-d$ hopping parameters t_3 and \tilde{t} on the magnetic interactions can be understood in terms of filling of the t_{2g} or e_g orbitals (see Fig. 2(a)) according to the Goodenough-Kanamori-Anderson (GKA) rules^{34,35}. In particular, hopping between half-filled orbitals is associated with antiferromagnetic exchange, while hopping from a half-filled to a full or empty orbital is associated with ferromagnetic exchange.

For the d^8 materials (i.e. NiX_2), we generally expect the nearest neighbor couplings to be ferromagnetic: the t_{2g} levels are filled; hence, the hopping processes involving t_3 do not contribute to exchange in lowest order. Therefore, J_1 arises mainly from \tilde{t} processes, which connect a half-filled e_g orbital to a filled t_{2g} orbital, and leads to a ferromagnetic exchange. This effect is enhanced in systems with heavier ligands, as the ligand-assisted \tilde{t} is strengthened by increased $p-d$ hybridization.

For the d^3 materials (i.e. VX_2), there is a competition between ferromagnetic (FM) and antiferromagnetic (AFM) contributions to the nearest neighbor exchange. In addition to the ferromagnetic exchange arising from the \tilde{t} process connecting an empty e_g with a half-filled t_{2g} orbital, an antiferromagnetic contribution arises from the hopping between the two half-filled t_{2g} orbitals via t_3 . While both mechanisms are relevant, the ferromagnetic contributions are typically weaker than antiferromagnetic contributions, so that $J_1 > 0$ (in part, because

X	VX_2			MnX_2			NiX_2		
	Cl	Br	I	Cl	Br	I	Cl	Br	I
U_{avg}	4.69	4.10	3.15	4.56	3.88	3.29	4.57	3.90	3.24
J_{avg}	0.65	0.63	0.57	0.79	0.75	0.71	0.84	0.79	0.68

TABLE I. Constrained RPA results of averaged Hubbard repulsion U_{avg} (in eV) and averaged Hund’s coupling J_{avg} (in eV) for the monolayer structures of each investigated material.

$|t_3| > \tilde{t}$). For heavier ligands, the increasing \tilde{t} should enhance the ferromagnetic contribution primarily, resulting in a decreased magnitude of J_1 .

Finally, for the high spin d^5 case (i.e. MnX_2), the overall magnitude of the couplings is generally expected to be weak. While both \tilde{t} and t_3 hopping processes contribute with antiferromagnetic contributions due to half-filled t_{2g} and e_g levels, their effects are reduced by two main factors. First, the energy cost for transfer of an electron between metal sites is the largest for the case of half filling⁴⁴. This can be understood by considering the effects of Hund's coupling; for a process $(\uparrow\uparrow\uparrow\uparrow, \downarrow\downarrow\downarrow\downarrow) \rightarrow (\uparrow\uparrow\uparrow\uparrow, \downarrow\downarrow\downarrow\downarrow\uparrow)$, the total Coulomb repulsion experienced by the electron at its parent site is mitigated by the spin alignment through Hund's coupling. After hopping, the electron's spin is necessarily anti-aligned with all other electrons, so that the full Coulomb repulsion is felt. For this reason the cost for electron transfer is large $\sim U + 4J$. This suppresses the antiferromagnetic exchange sufficiently that ferromagnetic exchange processes not captured in the d -only picture are competitive, resulting in an overall suppression of the nearest neighbor interactions. Full discussion of this situation is provided in the following sections.

C. Anisotropic Interactions

In this work, we consider d^3 , high-spin d^5 , and d^8 filling because the ground states possess no orbital degeneracy, and the orbital angular momentum is quenched at zeroth order. In addition, the atomic spin-orbit coupling for third row metals is relatively weak. For this reason, magnetic anisotropy associated with the metal alone is mostly negligible, allowing the effects of introducing heavy ligands to be investigated in detail. We discuss these effects again in terms of the effective d -only model, where the atomic SOC of the ligands ($\mathcal{H}_{\text{SOC}} = \xi \sum_l \mathbf{L}_l \cdot \mathbf{S}_l$) is downfolded into effective d - d hopping and on-site terms. Such terms can be estimated via Wannier projection techniques applied to fully relativistic DFT calculations, as shown in the following sections. In general, such single-particle contributions then take the form:

$$\mathcal{H}_{\text{hop}} = \sum_{lm} \sum_{\alpha\beta} \underline{c}_{l\alpha}^T \{ t_{\alpha\beta}^{lm} \mathbb{I} + \frac{i}{2} (\vec{\lambda}_{\alpha\beta}^{lm} \cdot \vec{\sigma}) \} \underline{c}_{m\beta} \quad (3)$$

in terms of the Pauli matrices σ and electron annihilation operators on site l and orbital α , $\underline{c}_{l\alpha} = (c_{l\alpha\uparrow} \ c_{l\alpha\downarrow})$ and its transpose $\underline{c}_{l\alpha}^T$. Here, the $t_{\alpha\beta}^{lm}$ represent the regular spin-independent hopping and crystal field terms between orbital α at metal site l and β at site m . The vector $\vec{\lambda}_{\alpha\beta}^{lm}$ then parameterizes the complex spin-dependent terms resulting from spin-orbit coupling. For example, the contribution from the atomic SOC at the metal site M corresponds to $\vec{\lambda}_{\alpha\beta}^M = -i \xi_M \langle \alpha | \mathbf{L} | \beta \rangle$. With inclusion of heavy ligands with large SOC constants ξ , there are two main effects.

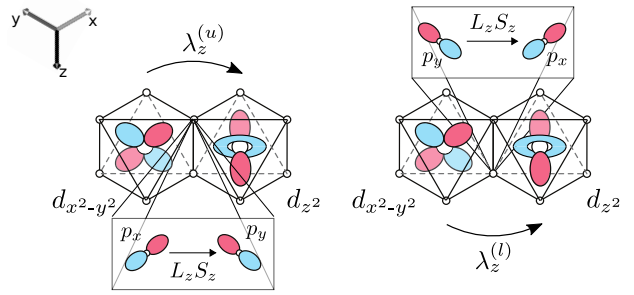


FIG. 3. Illustration of predominant nearest-neighbor spin-dependent hopping λ_z , arising from spin-orbit coupling effects on a Z_1 -bond (defined in Fig. 3). It results from the hopping along the upper ($\lambda_z^{(u)}$) and lower ($\lambda_z^{(l)}$) paths: $\lambda_z = \lambda_z^{(u)} + \lambda_z^{(l)}$.

The first effect is to induce spin-dependent crystal field terms as a result of p - d hybridization that mimic the atomic SOC. For example, the metal d_{xy} orbital may hybridize with the ligand p_y orbital, while the d_{xz} hybridizes with the ligand p_z orbital. The effects of SOC at the ligand is then to make an effective matrix element between the d -orbitals via the sequence $d_{xy} \xrightarrow{\text{hop}} p_y \xrightarrow{L_x S_x} p_z \xrightarrow{\text{hop}} d_{xz}$. When downfolded into the d -only picture, this mimics the effects of $L_x S_x$, with an effective SOC constant that scales with the atomic constant of the ligand and the degree of metal-ligand hybridization. However, as discussed further in Appendix C, the matrix elements of the induced SOC are not restricted to take the atomic form. They are the primary source of single-ion anisotropy (SIA), but the effects are difficult to anticipate *a priori*. We can anticipate only that the SIA should generally grow for heavier ligands. Experimentally, $3d^3$ and $3d^5$ materials tend to have weak single-ion anisotropy, while larger variations are seen for $3d^8$ materials⁴⁵.

The second effect concerns complex hopping between sites. The GKA rules can be modified to treat complex hoppings. For bonds with inversion symmetry, contributions at order $t\lambda$ in perturbation theory vanish precisely. Interactions arising at order $(\lambda)^2$ take the form $J_\mu (2S_l^\mu S_m^\mu - \mathbf{S}_l \cdot \mathbf{S}_m)$, where μ refers to the direction of $\vec{\lambda}$. The sign of J_μ is the same as anticipated from the GKA rules. Thus, spin-dependent hopping between half-filled orbitals results in an antiferromagnetic Ising term plus a ferromagnetic Heisenberg term of half the magnitude. The converse applies to hopping from half-filled orbitals to filled or empty orbitals. For all edge-sharing materials, the largest nearest neighbor $\vec{\lambda}_{\alpha\beta}^{lm}$ terms correspond to hopping between the e_g orbitals, which tend to hybridize with the ligands to a much higher degree than the t_{2g} orbitals. As a representative example, there are two relevant sequences for the Z_1 bond: $d_{x^2-y^2} \xrightarrow{\text{hop}} p_x \xrightarrow{L_z S_z} p_y \xrightarrow{\text{hop}} d_{z^2}$ ($\lambda_z^{(u)}$), via the upper path depicted in Fig. 3) and $d_{x^2-y^2} \xrightarrow{\text{hop}} p_y \xrightarrow{L_z S_z} p_x \xrightarrow{\text{hop}} d_{z^2}$ ($\lambda_z^{(l)}$), via the lower path). Due to the specific phases of the or-

bitals, these paths add constructively, $\lambda^z = \lambda_z^{(u)} + \lambda_z^{(l)}$. Within the spin-dependent hopping picture, this manifests into a particularly large $\lambda_{(x^2-y^2, z^2)}$. As discussed previously in Ref. 30, this may be associated with an antiferromagnetic Kitaev coupling for d^8 filling.

More generally, we expect strong bilinear anisotropic terms in materials with half-filled e_g orbitals, provided the ligands are sufficiently heavy. This applies most readily to d^8 filling, since materials with d^5 filling have reduced p - d hybridization. In contrast, the d^3 materials, with empty e_g orbitals, are expected to exhibit much weaker anisotropic exchange. The above trends and mechanisms highlight that electron filling and bonding geometry play crucial roles in the relative anisotropy of the magnetic couplings.

IV. MAGNETIC EXCHANGE COUPLINGS FOR MONOLAYER MX_2

In this section, we present estimates for the magnetic exchange couplings in monolayer MX_2 by employing the *ab-initio*-based projED and 4-state methods, and discuss results with the expected trends introduced above. The 4-state method is based on total energy mapping through non-collinear, magnetic DFT calculations, including SOC. Each magnetic interaction parameter is related to the energies of four distinct magnetic configurations^{32,33}. The projED method consists of two steps: i) a finite-cluster Hubbard Hamiltonian is constructed based on Wannier projection of a non-magnetic, relativistic band structure calculation; ii) the Hubbard Hamiltonian is solved via exact diagonalization (ED) and the corresponding effective spin Hamiltonian is extracted through projection onto the low-energy subspace³¹. In the results below, we employ a d -only basis for projED; as such, the effects of p - d hybridization are downfolded into effective d -only single particle terms and renormalized Coulomb terms discussed in Section III A. While this allows to capture the majority of contributions to the magnetic exchange, as recently pointed out for the d^7 case⁴⁶, there is one important contribution omitted, which represents the regular ferromagnetic Goodenough-Kanamori exchange for 90° bonds. This consists of processes where a hole from each metal site meets on a single ligand in different orbitals, and interact via Hund's coupling. Perturbative corrections due to this process are mentioned in each section. Further descriptions of both methods and their relative merits are provided in Appendix B.

In Appendix E we list results obtained with alternative U_{avg} and J_{avg} values for all nine investigated materials with both methods. These values were previously used by some of the authors in other works on the NiX_2 materials^{26,47}. The comparison to the results below highlights the independence of the qualitative trends obtained by the two employed methods on these input parameters.

NiX_2	projED			4-states		
	$NiCl_2$	$NiBr_2$	NiI_2	$NiCl_2$	$NiBr_2$	NiI_2
J_1	-0.7	-0.8	-1.2	-2.9	-3.9	-6.2
K_1	0.	+0.1	+1.0	0.	+0.2	+2.2
Γ_1	0.	0.	0.	0.	0.	0.
Γ'_1	0.	0.	-0.1	0.	0.	-0.1
J_2	0.	0.	0.	-0.1	-0.1	-0.2
J_3	+0.6	+1.0	+1.8	+0.8	+1.8	+4.2
A_c	0.	+0.1	+0.8	0.	0.	+0.4

TABLE II. Exchange parameters (in meV) for the NiX_2 monolayer structures using the respective ($U_{\text{avg}}, J_{\text{avg}}$) parameters determined with cRPA for each material (see Table I); extracted with the projED method (left) and the 4-states energy mapping method (right). Note that for the projED method J_1 should be corrected with $\delta J_1 \sim -2$ to -5 meV to take additional ferromagnetic contributions into account (see Appendix B).

A. d^8 $S = 1$ materials NiX_2

Experimentally, all bulk NiX_2 materials exhibit magnetic long-range order and were subject of intense investigation a few decades ago due to their metamagnetic and multiferroic behavior^{22,23,48,49}. For the monolayer structures, previous theoretical analysis by some of the authors indicated a range of possible ground states: from a topological spin lattice⁴⁷, composed of vortices and anti-bi-vortices to other competing commensurate and incommensurate phases^{47,50,51}, including a multiferroic spin spiral state²⁶.

In Table II, we report the exchange parameters of model Eq. (1) as defined in Eq. (2) for NiX_2 monolayers. Values are computed using the projED and 4-state methods, employing U_{avg} and J_{avg} values estimated via the cRPA approach (Table I).

In agreement with the expectations addressed in Section III, we find J_1 to be ferromagnetic (i.e. $J_1 < 0$) and increasing across the series Cl-Br-I due to increased metal-ligand hybridization. In d^8 materials, with half-filled e_g orbitals, exchange processes with multiple holes on a single ligand lead to significant ferromagnetic corrections to the value of J_1 obtained with projED. As detailed in Appendix B, we estimate with perturbation theory $\delta J_1 \sim -2$ to -5 meV. It should therefore be noted that the ferromagnetic ligand-mediated exchange δJ_1 is for d^8 filling the largest contribution to J_1 . This can be expected because the e_g orbitals hybridize strongly with the p -orbitals. The signs and overall magnitudes obtained for the monolayers are compatible with the bulk values; for example, bulk $NiCl_2$ orders ferromagnetically in plane^{48,52,53}, with ESR and neutron scattering experiments estimating $J_{1,\text{bulk}} \approx -3.6$ meV.

In both theoretical approaches, we find that the nearest neighbor anisotropic exchange is well represented by an antiferromagnetic Kitaev term K_1 , which may be quite substantial compared to J_1 in $NiBr_2$ and NiI_2 . The mag-

nitude of K_1 scales with the SOC strength of the ligand, clearly identifying the origin of the interaction as the hopping process depicted in Fig. 3. These findings are compatible with previous work on superexchange processes mediated by p -orbital anions with strong SOC³⁰, such as the $S = 1$ NiI₂ or the $S = 3/2$ Cr³⁺ monolayer systems^{15,54}. For example, Ref. 30 anticipated significant AFM Kitaev interactions in d^8 compounds. In that case a subset of exchange processes were considered, leading to the prediction $K_1 \gtrsim 2|J_1|$. Here, we find that the previously omitted correction δJ_1 somewhat reduces this ratio, but relatively large AFM Kitaev interactions still seem to be realised in NiI₂.

For the longer range couplings, a vanishingly small J_2 and significant antiferromagnetic J_3 , *i.e.* $|J_1| > |J_3| \gg |J_2|$, is found in both methods. These results can again be understood by considering the dominant hoppings. For the second and third nearest neighbors we discuss the Z_2 - and Z_3 -bonds, defined in Fig. 1(a). The hoppings between sites on a Z_2 -bond are dominated by $\tilde{t} = t_{(xy,z^2)}$ and $t_2 = t_{(xz,yz)}$. For the Z_3 -bond we find $t_3 = t_{(xy,xy)}$, $t_5 = t_{(x^2-y^2,x^2-y^2)}$, and $t_6 = t_{(z^2,z^2)}$ to be the largest. For second neighbors, the d^8 filling ensures that only the t_{2g-e_g} hopping \tilde{t} is relevant, which leads to a weak ferromagnetic interaction. This contribution is expected to be smaller than the nearest neighbor coupling by a factor $\sim (t_{2nn}/t_{nn})^2$, which explains the relative suppression. In contrast, for third neighbors, there are large e_g-e_g hoppings that arise from ligand-assisted hopping paths such as $d_{x^2-y^2} \xrightarrow{\text{hop}} p_x \xrightarrow{\text{hop}} p_y \xrightarrow{\text{hop}} d_{x^2-y^2}$ that are enhanced by metal-ligand hybridization and the spatial extent of the ligand p -orbitals. This results in large third neighbor t_5 and t_6 , producing significant third neighbor antiferromagnetic couplings, which tend to increase in magnitude across the series Cl-Br-I. In fact, with both projED and 4-state approaches, we find that $J_3/|J_1|$ increases toward a significant contribution across this series.

Regarding the single-ion anisotropy A_c , with both projED and 4-states methods, we generally find $A_c > 0$, with a magnitude that increases with the SOC strength of the ligand. This is compatible with bulk trends. For bulk NiCl₂, the single-ion anisotropy was determined to be finite, but small, *i.e.* below 0.01 meV^{48,53}. For bulk NiBr₂, SIA was experimentally⁵⁵ estimated to be larger $A_c \sim 0.08 \pm 0.05$ meV, which is similar to the monolayer projED estimation $A_c \approx 0.1$ meV. While it is tempting to attribute this effect to an increase in the effective SOC of the metal via d - p hybridization, the situation is not so simple, as outlined in Appendix C.

The classical ground states of the triangular Heisenberg model with isotropic ferromagnetic J_1 and competing FM or AFM J_2, J_3 have been thoroughly investigated in the past⁵⁶. Our estimated range of parameters are compatible with two possible magnetic ground states for NiX₂ monolayers, namely a ferromagnetic or an incommensurate helix with ordering wavevector $q_{2D} = (q, q)$, the latter displaying lower energy when $4J_3 \gtrsim |J_1| + 3|J_2|$. The increasing trend of $J_3/|J_1|$ across the Cl-Br-I series

indicates an enhanced tendency to stabilise incommensurate helimagnetism for heavier ligands, with NiCl₂ monolayer being very close to the FM-spiral phase boundary. These trends can be compared to their bulk counterparts, keeping in mind that interlayer interactions may also affect the magnetic properties of the latter.

Bulk NiCl₂ orders ferromagnetically in the plane^{48,52,53} with an ordering wavevector $q_{3D} = (0, 0, 1.5)$ signalling AFM interlayer interaction between the planes. On the other hand, NiBr₂ and NiI₂ undergo a series of transitions: upon decreasing temperature, they both enter first a similar state to bulk NiCl₂ of antiferromagnetically coupled ferromagnetic sheets^{49,57-61}, but then upon decreasing T further, they enter another, incommensurate spiral phase^{55,57-64}. For NiBr₂, the spiral displays a wavevector $(q, q, 1.5)$ with small $q \sim 0.03$ and spins lying in the plane of the layer^{55,58}. Such a phase can be understood in the context of a model with ferromagnetic J_1 , antiferromagnetic J_3 , and $A_c > 0$ with $J_3/|J_1| \gtrsim 0.25$ ⁵⁶, as well as antiferromagnetic interlayer exchange⁵⁵, thus demonstrating a significant $J_3 > 0$ in the bulk materials. These parameter trends are fully consistent with our monolayer calculations.

For bulk NiI₂, the spiral develops concomitantly with a structural transition from rhombohedral to monoclinic cell and displays instead a wavevector $(q, 0, \sim 1.46)$, with $q \gtrsim 0.1$ and moments oriented in the plane perpendicular to one of the cubic axes ($\sim 35^\circ$ from the plane)⁶¹. Such an orientation is difficult to understand without invoking bond-dependent couplings referenced to the cubic axes. Since the ordering vector is perpendicular to a bond, the ordering pattern consists of stripes in which moments linked by one of the nearest neighbor bond types are always aligned in parallel. In the presence of a sizeable antiferromagnetic $K_1 > 0$, there is an energetic preference for the moments to align in the plane perpendicular to the associated cubic axis of the bond perpendicular to the q -vector. This is precisely what is observed experimentally. Thus the particular moment orientation should be taken as evidence for significant $K_1 > 0$ in bulk NiI₂. Albeit the larger ordering wavevector of bulk NiI₂ is still consistent with our prediction of increasing magnetic frustration across the Cl-Br-I series, the in-plane component of bulk q_{3D} would suggest, within an isotropic Heisenberg model, a strong antiferromagnetic J_2 ^{56,61}. Such a significant deviation from expected and estimated trends for magnetic interactions in the NiX₂ class is difficult to rationalize, and one may wonder how appropriate it is to compare bulk and monolayer NiI₂. A recent experimental analysis of NiI₂ magnetic properties down to the monolayer limit via complementary optical techniques could not resolve the 2D ordering wavevector, both $q_{2D} = (q, q)$ and $(q, 0)$ being compatible with the detected symmetries²⁶. At the same time, a quite strong AFM interlayer interaction, $\sim 0.45|J_1|$, was deduced from the layer-dependent spiral transition temperature²⁶, much larger than the interlayer exchange of NiBr₂, $\sim 0.1|J_1|$ ⁵⁵. These facts suggest that other mechanisms, not included in the 2D model

VX ₂	projED			4-states		
	VCl ₂	VBr ₂	VI ₂	VCl ₂	VBr ₂	VI ₂
J ₁	+4.9	+3.6	+2.6	+4.2	+2.5	+0.6
K ₁	0.	0.	0.	0.	0.	-0.1
Γ ₁	0.	0.	0.	0.	0.	+0.1
Γ' ₁	0.	0.	0.	0.	0.	0.
J ₂	0.	+0.1	+0.1	0.	0.	+0.1
J ₃	0.	+0.1	+0.1	0.	+0.1	+0.2
A _c	0.	0.	0.	0.	0.	0.

TABLE III. Exchange parameters (in meV) for the VX₂ monolayer structures using the respective ($U_{\text{avg}}, J_{\text{avg}}$) parameters determined with cRPA for each material (see Table I); extracted with the projED method (left) and the 4-states energy mapping method (right).

considered here, may play an important role in shaping the bulk magnetic properties of NiI₂.

Finally, we note that a large nearest neighbor bi-quadratic exchange $B(\mathbf{S}_i \cdot \mathbf{S}_j)^2$ with $B < 0$ was recently invoked to explain the collinear ground state of NiCl₂, compared to non-collinear helimagnetic ground states of NiBr₂ and NiI₂. To test the possibility of large B , we also computed all higher order couplings using projED for the monolayer structure, which is capable of capturing 4-spin interactions⁶⁵. However, we find no 4-spin terms exceeding 0.01 meV. This result can be understood from the fact that B arises at order t^4/U^3 in perturbation theory, and is generally expected to be significant for nearly itinerant electrons. Nonetheless, it could still be relevant for systems like NiCl₂ that are at the verge of the FM-spiral phase transition and, as such, sensitive to other weak interactions not included in the model Eq. (1).

B. d^3 $S = 3/2$ materials VX₂

For VX₂ compounds, the exchange parameters extracted with both *ab-initio* methods are given in Table III. Good agreement is found both in magnitude and trends between 4-state and projED approaches.

We find antiferromagnetic (AFM) nearest neighbor Heisenberg coupling J_1 , with a decreasing magnitude as a function of the ligand atomic number. As outlined in Section III, the dominant hopping processes suggest a competition between antiferromagnetic and ferromagnetic contributions in VX₂, resulting in a net antiferromagnetic interaction; the ligand-assisted hoppings become more important for the heavier ligands, leading to a stronger contribution of the ferromagnetic exchange and resulting in the overall decrease of $|J_1|$ across the series Cl-Br-I.

The second and third nearest neighbor couplings, J_2 and J_3 respectively, turn out to be small generally. This can be understood considering the primary third neighbor hopping occurs between e_g orbitals via paths like

$e_g \xrightarrow{\text{hop}} p \xrightarrow{\text{hop}} p \xrightarrow{\text{hop}} e_g$. For d^3 filling, such hoppings are irrelevant to the magnetic couplings. As a result, the long-range interactions are suppressed compared to d^8 filling. Similarly, consistent with the discussion in Section III, the bilinear anisotropic exchange is negligible, since the ligand SOC only makes relevant corrections to hopping between e_g orbitals.

Our results show consistency with behaviors experimentally observed in the VX₂ bulk systems. Estimated intralayer nearest-neighbor exchange couplings fitting data from susceptibility⁶⁶ and INS data^{67,68}, were reported to be $J_1 = +3.8$ meV and $J_1 = +2.8$ meV, for bulk VCl₂ and VBr₂, which supports the *ab-initio* trends. Moreover, the AFM Néel 120° spin order was observed, with transition temperatures of $T_N = 36$ K and 29 K, for the two systems respectively⁶⁷⁻⁷⁰. In accordance with our *ab-initio* intralayer estimates, these results suggest that monolayer VCl₂ and VBr₂ can be sufficiently described by short-range AFM interactions. Given the absence of anisotropic couplings, we would expect these ordering temperatures to be significantly reduced in monolayers. However the ordering pattern is not expected to differ.

At variance, the physics of VI₂ appears less obvious. Bulk VI₂ displays AFM 120° correlations at high temperature, but ultimately orders at $T_N = 14.4$ K into an AFM collinear zigzag stripe order^{69,71}. No experimental estimates of J_1 are available (to the best of our knowledge). However, the lower T_N values with respect to VCl₂ and VBr₂ suggest reliability of our *ab-initio* estimates: the former suggests energetic competition between AFM phases that could be ascribed to the non-zero intralayer J_3 contribution estimated in monolayer VI₂; the latter supports the argued J_1 decrease across the series Cl-Br-I (Table III).

C. $S = 5/2$ materials MnX₂

As discussed in Section III, the magnetic exchange interactions in MnX₂ are expected to be relatively suppressed as a consequence of the large energy cost for transfer of electrons between metal sites. This is indeed what is found with both projED and 4-state approaches, as detailed in Table IV. Due to the partially filled e_g orbitals, J_1 obtained with projED has to be corrected, with $\delta J_1 \sim -0.4$ to -0.9 meV (see Appendix B). The nearest-neighbor Heisenberg J_1 exchange is found to be antiferromagnetic, with little variation with ligand elements, in contrast to the behaviors discussed for NiX₂ and VX₂. Anisotropic exchange associated with the $e_g \xrightarrow{\text{hop}} p \xrightarrow{\text{hop}} p \xrightarrow{\text{hop}} e_g$ hopping processes should be finite, but it represents only a small fraction of the total contributions, and is therefore negligible. With both approaches we find longer range couplings J_2 and J_3 in the range 0.01 to 0.1 meV, which may be significant given the relative suppression of J_1 .

Consistently with the nearly suppressed magnetic exchange interactions, very low experimental transition

MnX ₂	projED			4-states		
	MnCl ₂	MnBr ₂	MnI ₂	MnCl ₂	MnBr ₂	MnI ₂
J_1	+0.8	+0.7	+0.7	+0.1	+0.1	+0.1
K_1	0.	0.	0.	0.	0.	0.
Γ_1	0.	0.	0.	0.	0.	0.
Γ'_1	0.	0.	0.	0.	0.	0.
J_2	0.	0.	0.	0.	0.	0.
J_3	0.	+0.1	+0.1	0.	0.	+0.1
A_c	0.	0.	0.	0.	0.	0.

TABLE IV. Exchange parameters (in meV) for the MnX₂ monolayer structures using the respective ($U_{\text{avg}}, J_{\text{avg}}$) parameters determined with cRPA for each material (see Table I); extracted with the projED method (left) and the 4-states energy mapping method (right). Note that for the projED method J_1 should be corrected with $\delta J_1 \sim -0.4$ to -0.9 meV to take additional ferromagnetic contributions into account (see Appendix B).

temperatures are reported for the bulk MnX₂ systems. Particularly, bulk MnCl₂ and MnBr₂ exhibit two successive transitions at $T_{N_1} = 1.96$ K, $T_{N_2} = 1.81$ K⁷² and $T_{N_1} = 2.32$ K, $T_{N_2} = 2.17$ K⁷³⁻⁷⁵ respectively. In both cases, the intermediate phase has been identified as an incommensurate phase, and the low-temperature structure as a double stripe order phase. Bulk MnI₂ exhibits even three subsequent magnetic transitions below 4 K^{73,75}. The lowest temperature phase was identified as a spiral order with an incommensurate wavevector⁷⁶. Given the very small magnitude of the exchange couplings and large $S = 5/2$, we agree with previous speculations^{75,77} that long-range dipolar interactions may ultimately be relevant for both, bulk and monolayer systems.

V. CONCLUSIONS

With this study we investigated the effective magnetic models in the monolayer family of triangular lattice materials MX_2 ($M=\{\text{V, Mn, Ni}\}$, $X=\{\text{Cl, Br, I}\}$), where spin-orbit coupling effects are dominantly caused by the ligand element. We also took the opportunity of such a larger study to benchmark two *ab-initio* methods used to extract effective spin models for real materials.

Considering the very different nature of the two *ab-initio*-based methods considered here, the results agree remarkably well in terms of signs and trends in the relative magnitudes. The points of disagreement are typically the overall magnitude. Among others, this may be assigned to the implementation of the parameter values U_{avg} and J_{avg} , since they enter either in the Hubbard Hamiltonian for projED, or in the DFT+U framework for the 4-states method. For consistency, we compared both methods using the same parameter values in spite of the fact that this may not be the ideal parameter set especially for the 4-states method. On the other hand, in the 4-states method an overall linear dependence vary-

ing these parameters was found (compare Table IX) while the projED method relies stronger on choosing appropriate parameter sets such as the ones used in this work, obtained with cRPA. In the case of half-filled e_g orbitals for the projED method ferromagnetic contributions from additional processes have to be considered, which we estimated here via perturbation theory.

Regarding the magnetic parameters for the triangular lattice compounds in general, we find trends for the monolayer structures consistent with expectations based on experimental observations in the bulk case. Noticeably, for monolayer NiI₂ we do find sizeable Kitaev coupling suggested in previous works^{30,47}, as well as large ferromagnetic J_1 and significant antiferromagnetic J_3 isotropic couplings. The VX₂ monolayer structures can all be described well in the framework of nearest neighbor AFM Heisenberg models, and the MnX₂ materials reveal overall suppressed magnetic exchange, hinting at long-range dipolar interactions as potentially the most important factor for the magnetic ground state.

Finally, already the use of simplified models made it possible to understand the underlying mechanism of the magnetic exchange in the triangular MX_2 compounds. Consideration of two dominant hopping parameters enabled us to identify the (anti-)ferromagnetic nature of J_1 in the (d^3) d^8 materials, including the trends of additional or competing ferromagnetic contributions for larger ligands. Our analysis further allows for a physical insight in the peculiar situation of d^8 materials, displaying i) significant enhancement of the third-nearest-neighbor exchange interaction J_3 , especially when compared to shorter-range J_2 , and ii) substantial anisotropic exchange/Kitaev interactions, increasing with ligand atomic number. The first effect can be understood only if the specific hopping interactions and involved orbital states contributing to the exchange interactions are properly taken into account: as the hopping processes relevant for J_2 and J_3 are fundamentally different, the conventional expectation that exchange interaction should roughly scale with the inverse of the bond length is, at best, inaccurate. Additionally, J_3 is dominated by ligand-assisted hopping processes, and as such can be directly tuned by the metal-ligand hybridization (hence by appropriate choices of the ligand). Similarly, relativistic anisotropic exchanges arise mostly from ligands spin-orbit coupling, which tunes through ligand-assisted hoppings the effective SOC between the magnetic ions and strongly modifies its matrix elements as compared to the atomic limit. It follows that the resulting strength of the anisotropic exchange found in d^8 materials is mostly driven by the atomic SOC of the ligands, as well as by the metal-ligand hybridization again. The emerging picture thus possibly suggests strategies to enforce magnetic frustration and Kitaev-type interactions, both sought for in the quest of exotic magnetic phases, alternative to existing ones based mostly on suitable choices of heavier ($4d$ or $5d$) transition metals.

ACKNOWLEDGMENTS

R.V. and K.R. acknowledge support by the Deutsche Forschungsgemeinschaft (DFG, German Research Foundation) for funding through TRR 288 — 422213477 (projects A05 and B05). D.A. and S.P. acknowledge support by the Nanoscience Foundries and Fine Analysis (NFFA-MIUR Italy) project. P.B. and S.P. acknowledge financial support from the Italian Ministry for Research and Education through PRIN-2017 projects ‘Tuning and understanding Quantum phases in 2D materials—Quantum 2D’ (IT-MIUR grant No. 2017Z8TS5B) and ‘TWEET: Towards ferroelectricity in two dimensions’ (IT-MIUR grant No. 2017YCTB59), respectively. D.A., P.B. and S.P. also acknowledge high-performance computing systems operated by CINECA (IsC722DFmF, IsC80-Em2DvdWd, IsC88-FeCoSMO and IsB21-IRVISH projects). D.A. is grateful to M. Verstraete and B. Dupé (ULiege) for the time allowed to work on the writing of this paper.

Appendix A: Relation between exchange values in crystallographic and cubic coordinate systems

The parameterization convention used in the main text follows the extended Heisenberg-Kitaev model with focus on the bond-dependent Ising-like Kitaev interaction. With this convention it is easy to identify such general bond-dependent parameters. For example, on a Z_1 -bond between sites l and m , the magnetic exchange matrix is defined as follows:

$$\mathbb{J}_{lm}^{Z_1} = \begin{pmatrix} J & \Gamma & \Gamma' \\ \Gamma & J & \Gamma' \\ \Gamma' & \Gamma' & J + K \end{pmatrix}. \quad (\text{A1})$$

while on an X_1 -bond it can be determined by C_3 rotation about the out-of-plane axis arriving at:

$$\mathbb{J}_{lm}^{X_1} = \begin{pmatrix} J + K & \Gamma' & \Gamma' \\ \Gamma' & J & \Gamma \\ \Gamma' & \Gamma & J \end{pmatrix}. \quad (\text{A2})$$

Alternatively, the interactions can also be expressed in a coordinate system oriented along the crystal axes (ab^*c), where b^* is perpendicular to a and c . By symmetry, the magnetic exchange on a bond along the a axis (e.g. Z_1 -bond) can be parametrized with:

$$\mathbb{J}_{lm}^{Z_1} = \begin{pmatrix} J_{aa} & 0 & 0 \\ 0 & J_{b^*b^*} & J_{b^*c} \\ 0 & J_{b^*c} & J_{cc} \end{pmatrix}. \quad (\text{A3})$$

The corresponding exchange matrix on the X_1 -bond can then be again obtained by C_3 rotation about the c axis:

$$\mathbb{J}_{lm}^{X_1} = \begin{pmatrix} \frac{1}{4}(J_{aa} + 3J_{b^*b^*}) & -\frac{\sqrt{3}}{4}(J_{aa} - J_{b^*b^*}) & -\frac{\sqrt{3}}{2}J_{b^*c} \\ -\frac{\sqrt{3}}{4}(J_{aa} - J_{b^*b^*}) & \frac{1}{4}(3J_{aa} + J_{b^*b^*}) & -\frac{1}{2}J_{b^*c} \\ -\frac{\sqrt{3}}{2}J_{b^*c} & -\frac{1}{2}J_{b^*c} & J_{cc} \end{pmatrix}. \quad (\text{A4})$$

Both approaches are equivalent and can be directly translated into each other via the following relations:

$$J = \frac{1}{6} \left(3J_{aa} + J_{b^*b^*} + 2J_{cc} + 2\sqrt{2}J_{b^*c} \right) \quad (\text{A5})$$

$$K = \frac{1}{2} \left(-J_{aa} + J_{b^*b^*} - 2\sqrt{2}J_{b^*c} \right) \quad (\text{A6})$$

$$\Gamma = \frac{1}{6} \left(-3J_{aa} + J_{b^*b^*} + 2J_{cc} + 2\sqrt{2}J_{b^*c} \right) \quad (\text{A7})$$

$$\Gamma' = \frac{1}{6} \left(-2J_{b^*b^*} + 2J_{cc} - \sqrt{2}J_{b^*c} \right) \quad (\text{A8})$$

Independent of the coordinate system, the exchange matrix can conventionally be decomposed into three distinct contributions. The fully isotropic part with respect to spin orientations—in contrast to bond anisotropy—corresponds to $J_{lm}^{\text{iso}} = \frac{1}{3}\text{Tr}(\mathbb{J}_{lm})$. In the case of the cubic coordinate system with Eq. (A1), this would correspond to $J_{lm}^{\text{iso}} = J + K/3$. The anisotropic terms with respect to spin orientation are composed of the symmetric term, $\mathbb{J}_{lm}^{\text{S}} = \frac{1}{2}(\mathbb{J}_{lm} + \mathbb{J}_{ml}) - J_{lm}^{\text{iso}}\text{I}$ and the anti-symmetric term $\mathbb{J}_{lm}^{\text{A}} = \frac{1}{2}(\mathbb{J}_{lm} - \mathbb{J}_{ml})$. The latter vanishes in the presence of an inversion center in the middle of the bond, as it is the case for the materials investigated in this work.

Appendix B: Methods

1. Monolayer MX_2 structures

Within the projED and 4-state methods, calculations have been performed on fixed triangular MX_2 monolayer structures, which have been fully relaxed through structural relaxations as implemented in VASP⁷⁸, within the generalized gradient approximation (GGA) and Perdew–Burke–Erzenhof (PBE)³⁸ functional. Particularly, no Hubbard- U and SOC corrections were employed for all the structures’ optimization, whereas different magnetic orderings were considered according to calculated energetics (i.e. lowest energy configuration without SOC contribution): FM order for NiX_2 systems, consistent with previous works⁴⁷ and 120° AFM order for MnX_2 and VX_2 systems. The obtained in-plane lattice parameters ($|\mathbf{a}| = |\mathbf{b}|$) are reported in Table V; the c length was fixed to 20.8 Å, to insert a vacuum distance between periodic repetition of the layers along this direction.

	calc. exp. ⁷⁹		calc. exp. ⁷⁹		calc. exp. ⁷⁹			
NiCl ₂	3.49	3.48	VCl ₂	3.54	3.6	MnCl ₂	3.70	3.71
NiBr ₂	3.69	3.7	VBr ₂	3.75	3.77	MnBr ₂	3.88	3.89
NiI ₂	3.96	3.9	VI ₂	4.05	4.06	MnI ₂	4.15	4.15

TABLE V. In-plane lattice parameters in angstrom (Å) for the studied triangular MX_2 monolayer systems. Values obtained from DFT-calculations are compared with corresponding experimental data for bulk structures.

2. Constrained RPA

We estimated the electronic two-particle interaction terms with the constrained random-phase approximation (cRPA)^{39,40}, as implemented in the FHI-gap code⁸⁰. The approach is similar to a recent cRPA study⁸¹, applied here for the discussed relaxed monolayer structures and considering the full five $3d$ orbitals of the metal elements in each case. The atomic-like spherical symmetric expressions for d block electrons derived from Slater integrals⁸² F_k can be obtained via the following relations (for orbitals α, β and angular momentum quantum number l):

$$U_{\text{avg}} = \frac{1}{(2l+1)^2} \sum_{\alpha\beta} U_{\alpha\beta} = F_0, \quad (\text{B1})$$

$$J_{\text{avg}} = \frac{7}{5} \frac{1}{2l(2l+1)} \sum_{\alpha\neq\beta} J_{\alpha\beta} = \frac{F_2 + F_4}{14}. \quad (\text{B2})$$

3. ProjED

The projED method³¹ consists of two main steps. First, an effective electronic multi-orbital Hubbard Hamiltonian \mathcal{H}_{tot} is determined:

$$\mathcal{H}_{\text{tot}} = \mathcal{H}_{\text{hop}} + \mathcal{H}_{\text{U}}, \quad (\text{B3})$$

$$\mathcal{H}_{\text{hop}} = \sum_{lm} \sum_{\alpha\beta} \sum_{\sigma\sigma'} t_{l\alpha,m\beta}^{\sigma\sigma'} c_{l\alpha\sigma}^\dagger c_{m\beta\sigma'}, \quad (\text{B4})$$

$$\mathcal{H}_{\text{U}} = \sum_{l\alpha\beta\gamma\delta} \sum_{\sigma\sigma'} U_{l\alpha\sigma\sigma'\gamma\delta} c_{l\alpha\sigma}^\dagger c_{l\beta\sigma'}^\dagger c_{l\delta\sigma'} c_{l\gamma\sigma}, \quad (\text{B5})$$

where $\{l, m\}$ are site, $\{\alpha, \beta\}$ orbital and $\{\sigma, \sigma'\}$ spin indices. \mathcal{H}_{hop} describes non-magnetic hopping processes between the $3d$ electronic (spin-)orbitals of the transition metals $M = \{\text{Ni}, \text{V}, \text{Mn}\}$ and \mathcal{H}_{U} the respective two-particle Coulomb interaction. The hopping parameters were computed *ab-initio* using the Full Potential Local Orbital⁴³ (FPLO) code within the generalized gradient approximation³⁸ (GGA) for each monolayer structure. The hopping parameters are extracted via Wannier projection based on full relativistic non-spin-polarized band structures. This allows to effectively consider the influence of the heavy ligands involved, especially in the case of the MI_2 series, and results in *complex* hopping parameters. To ensure consistent treatment of the two-particle Coulomb interaction within the investigated series, the Coulomb parameters were extracted for each material within the cRPA method, as described above.

In a second step, an effective spin Hamiltonian is extracted:

$$\mathcal{H}_{\text{eff}} = \mathbb{P} \mathcal{H}_{\text{tot}} \mathbb{P} = \sum_{l\mu\nu} J_{l\mu\nu}^\mu S_l^\mu S_m^\nu \quad (\text{B6})$$

with $\mu, \nu \in \{x, y, z\}$. The projection operator \mathbb{P} projects the electronic Hamiltonian onto its low-energy subspace

and then maps onto the respective spin operator representation. The low-energy eigenstates, required for the first step, are computed via exact diagonalization of the five-orbital electronic Hamiltonian on finite two-site clusters. After reducing the Hilbert space onto an energetic regime where spin degrees of freedom are sufficient to describe the relevant physical properties, the Hamiltonian can be mapped from the electronic onto the spin picture using Stevens operators. In case of $S = 1/2$ this would correspond to the well-known Pauli matrices.

Estimating exchange parameters in the above introduced d -only basis, ferromagnetic corrections arising from exchange processes with multiple holes on a single ligand are omitted. These contributions are dominantly relevant for the isotropic interaction in materials with partially filled e_g orbitals, since p orbitals hybridize predominantly with e_g orbitals. We estimate δJ_1 for the relevant fillings via perturbation theory.

For d^8 filling, the ferromagnetic correction to the projED results can then be estimated by:

$$\delta J_1 = -\frac{1}{S^2} \frac{(t_{pd}^\sigma)^4 J_{\text{H}}^p}{\Delta_{pd}^2 (\Delta_{pd} + U_p/2)^2} \quad (\text{B7})$$

where Δ_{pd} is the charge transfer energy from d to p orbitals, U_p is the excess ligand Coulomb repulsion, J_{H}^p is the ligand Hund's coupling, and t_{pd}^σ is the e_g - p hopping integral in the Slater-Koster scheme. On the basis of non-relativistic band-structure calculations, we estimate $t_{pd}^\sigma \sim 1$ eV and $\Delta_{pd} \sim 3$ to 4 eV for NiX_2 , while we take $U_p \sim 4$ eV, $J_{\text{H}}^p \sim 0.3 U_p$ following Ref. 83.

For d^3 filling, the ferromagnetic correction can be approximated by:

$$\delta J_1 = -\frac{3}{S^2} \frac{(t_{pd}^\pi)^4 J_{\text{H}}^p}{\Delta_{pd}^2 (\Delta_{pd} + U_p/2)^2} \quad (\text{B8})$$

where we estimate the t_{2g} - p hopping $t_{pd}^\pi \sim 0.7$ eV, and $\Delta_{pd} \sim 4$ to 5 eV. Again, we may take $U_p \sim 4$ eV, $J_{\text{H}}^p \sim 0.3 U_p$ following Ref. 83. This provides an estimate of $\delta J_1 \sim -0.3$ to -0.7 meV. The correction is significantly reduced compared to the NiX_2 compounds due to the weaker t_{2g} - p hybridization. As a result, the couplings are well approximated by the d -only terms.

For d^5 filling, δJ_1 may be estimated via:

$$\delta J_1 = -\frac{1}{S^2} \frac{[(t_{pd}^\sigma)^4 + 2(t_{pd}^\sigma)^2 (t_{pd}^\pi)^2 + 3(t_{pd}^\pi)^4] J_{\text{H}}^p}{\Delta_{pd}^2 (\Delta_{pd} + U_p/2)^2}. \quad (\text{B9})$$

Taking $t_{pd}^\sigma \sim 1$ eV, $t_{pd}^\pi \sim 0.7$ eV, $\Delta_{pd} \sim 4$ to 5 eV, $U_p \sim 4$ eV, and $J_{\text{H}}^p \sim 0.3 U_p$ ⁸³ yields an estimate of the correction to $\delta J_1 \sim -0.4$ to -0.9 meV.

Extracting the local single-ion anisotropy, we considered a linked-cluster expansion including two-site clusters in order to take contributions from nearest neighbor interactions next to the local contributions into account.

For further neighbor interactions, two-site clusters are used with hopping parameters between the relevant sites.

Note that this procedure neglects contributions through indirect hopping paths that involve more than two magnetic sites, but is unavoidable for fillings approaching half-filling due to the computationally demanding exact diagonalization step. Especially for long-range interactions such as J_3 this approximation may be cautiously examined. For the NiX_2 series we tested the neglected contributions via linked cluster expansion, as used previously with projED⁸⁴, including up to three magnetic sites. At least for this class of materials we find only minor modifications below 1%.

4. 4-state total energies

The estimate of the magnetic interaction parameters employing the “4-state method” relies on DFT calculations of the total energies associated to various spin configurations to be mapped on the classical spin Hamiltonian written in Eq. (1). This approach is known as energy-mapping analysis. Specifically, the 4-state energy mapping method, which is explained in detail in Refs 15 and 32, allows us to extract the magnetic exchange interaction, both the isotropic and anisotropic contributions, between a selected pair of magnetic sites by performing DFT plus SOC energy calculations on four ordered non-collinear spin states. It is based on the use of supercells, which allow to exclude couplings with unwanted distant neighbors. The method is however tied to the choice of DFT basis, implementation of exchange correlation functional used in DFT and to specific computational parameters (i.e. k-points sampling, Hubbard U corrections within DFT+U, etc.).

In this work, we performed calculations of the SIA, first- and second-neighbors interaction using a $5 \times 4 \times 1$ supercell, while a $6 \times 3 \times 1$ supercell was used for the estimate of the third-neighbor interaction. Such large cells should exclude a significant influence from next neighbors. We built supercells from the periodic repetition of the MX_2 monolayer unit cell; structural details are reported in Sec. IV.

By means of this method we can obtain all the elements of the exchange tensor for a chosen magnetic pair, thus gaining direct access to the symmetric anisotropic exchange part (or two-ion anisotropy) and the antisymmetric anisotropic part (the DM interaction) of the full exchange. In particular, we performed direct calculations on the magnetic M - M pairs parallel to the crystallographic a direction (Fig. 1), determining the exchange tensor reported in Eq. (A3). The interaction between the five other nearest-neighbor pairs can be evaluated via the three-fold rotational symmetry, as in Eq. (A4). In all our systems, the tensor turned out to be symmetric or, equivalently, any anti-symmetric (DM-like) contribution was found to be negligible.

	generic Z-bond					Z ₁ -bond VCl ₂				
	d_{xy}	d_{xz}	d_{yz}	$d_{x^2-y^2}$	d_{z^2}	d_{xy}	d_{xz}	d_{yz}	$d_{x^2-y^2}$	d_{z^2}
d_{xy}	t_3	t_4	t_4	0	\tilde{t}	-248	10	10	0	121
d_{xz}	t_4	t_1	t_2	t_8	t_7	10	68	30	0	-3
d_{yz}	t_4	t_2	t_1	$-t_8$	t_7	10	30	68	0	-3
$d_{x^2-y^2}$	0	$-t_8$	t_8	t_5	0	0	0	0	-90	0
d_{z^2}	\tilde{t}	t_7	t_7	0	t_6	121	-3	-3	0	-2
	Z ₂ -bond VCl ₂					Z ₃ -bond VCl ₂				
	d_{xy}	d_{xz}	d_{yz}	$d_{x^2-y^2}$	d_{z^2}	d_{xy}	d_{xz}	d_{yz}	$d_{x^2-y^2}$	d_{z^2}
d_{xy}	1	-2	-2	0	16	-19	2	2	0	13
d_{xz}	-2	5	-13	2	2	2	2	-4	-2	-2
d_{yz}	-2	-13	5	-2	2	2	-4	2	2	-2
$d_{x^2-y^2}$	0	2	-2	-1	0	0	-2	2	56	0
d_{z^2}	16	2	2	0	1	13	-2	-2	0	-20

TABLE VI. Non-relativistic, non-spin-polarized hopping parameters for a generic Z-bond, considering only symmetry restrictions, as well as hopping parameters (in meV) for VCl₂ on a Z₁-, Z₂-, and Z₃-bond as defined in Fig. 1. The dominant hoppings are highlighted for Z₁ (t_3 , \tilde{t}), Z₂ (t_2 , \tilde{t}) and Z₃ (t_3 , t_5 , t_6).

Appendix C: Details of non-spin-polarized hopping parameters

To understand the microscopic mechanisms dictated by symmetry considerations of the space group $P\bar{3}m1$ (164) it is insightful to first consider the underlying electronic processes, which we model with an effective tight-binding Hamiltonian reduced on the magnetic ions M . The corresponding Hamiltonian is given in Eq. (B3). The hopping parameters discussed in this section were obtained using the Full Potential Local Orbital⁴³ (FPLO) code within the generalized gradient approximation³⁸ (GGA) and served in the relativistic case as basis for the projED results in the main text.

a. Effects without spin-orbit coupling

We first consider the case without spin-orbit coupling effects. In this case $t_{\alpha\beta}^{\sigma\sigma'} = t_{\alpha\beta}^{\sigma'\sigma} \delta_{\sigma\sigma'}$.

Let us consider the symmetry restrictions on first, second and third neighbor bonds, which can be all described by the same reduced matrices due to $2/m$ symmetry at their bond center. For this discussion, we focus on Z₁-, Z₂ and Z₃-bonds, which can be related to the other first, second and third neighbor bonds by the appropriate symmetry operations of the crystal. The Z₁ and Z₃ bonds are parallel to the crystallographic a direction, in cubic coordinates along $[1\bar{1}0]$ and the corresponding C_2 rotation axis is parallel to the bond. The Z₂ bond is perpendicular to that bond, in cubic coordinates along the $[11\bar{2}]$ direction. Since in this case the C_2 axis is perpendicular to the bond and in-plane, it turns out to be parallel to the C_2 axes of the Z₁ and Z₃ bond and the same restrictions

on the hopping matrices are valid in this case.

In Table VI we list the generic hopping matrix on a Z-bond with $2/m$ symmetry at the bond center. The hopping matrix between t_{2g} orbitals is fully determined by four parameters $t_{1\dots 4}$, following the convention introduced in Ref. 85. For a perfect octahedral geometry of the ligands $t_4 = 0$. In the materials considered, the octahedra do not deviate too strongly from a perfect shape, hence t_4 is generally small, as can be seen for the hopping parameters listed for the example case NiCl_2 . Following from the Slater-Koster integrals in a 90° M - X - M geometry⁴¹, t_2 is dominated by ligand-assisted hopping processes, while t_1 and t_3 arise mainly from direct hopping.

Hopping between t_{2g} and e_g orbitals is constrained to three parameters, \tilde{t} , t_7 , t_8 . However, if the considered bond lies within a mirror plane, t_7 and t_8 vanish. While this is not a symmetry of the crystal, it is a symmetry of a single bond Ni_2I_{10} molecule. In the crystal, these hoppings are hence finite, but small. Consequently, the ligand-assisted \tilde{t} dominates the exchange between t_{2g} and e_g orbitals.

Finally, hopping between e_g orbitals can be described with two parameters t_5 and t_6 , where the off-diagonal terms vanish due to the $2/m$ symmetry. These hoppings turn out to be important for further neighbor interactions on e.g. the Z_3 -bond.

b. Effects of spin-orbit coupling

As mentioned in the main text, the Hamiltonian $\mathcal{H}_{\text{hop}} = \sum_{lm} \sum_{\alpha\beta} c_{l\alpha}^\dagger \{t_{\alpha\beta}^{lm} \mathbf{I} + \frac{i}{2}(\vec{\lambda}_{\alpha\beta}^{lm} \cdot \vec{\sigma})\} c_{m\beta}$ is suitable to describe hopping processes including spin-orbit coupling effects. In Table VII, we list for the example case VI_2 the hopping parameters on-site and for the Z_1 -bond.

The on-site hopping parameters can be directly compared to the analytic expressions of the matrix elements in $\lambda_{\text{eff}} \mathbf{L} \cdot \mathbf{S}$ for d orbitals in the atomic limit:

$$\begin{array}{c|ccccc} \lambda_z & d_{xy} & d_{xz} & d_{yz} & d_{x^2-y^2} & d_{z^2} \\ \hline d_{xy} & 0 & 0 & 0 & 2\lambda_{\text{eff}} & 0 \\ d_{xz} & 0 & 0 & -\lambda_{\text{eff}} & 0 & 0 \\ d_{yz} & 0 & \lambda_{\text{eff}} & 0 & 0 & 0 \\ d_{x^2-y^2} & -2\lambda_{\text{eff}} & 0 & 0 & 0 & 0 \\ d_{z^2} & 0 & 0 & 0 & 0 & 0 \end{array} \quad (\text{C1})$$

$$\begin{array}{c|ccccc} \lambda_x & d_{xy} & d_{xz} & d_{yz} & d_{x^2-y^2} & d_{z^2} \\ \hline d_{xy} & 0 & -\lambda_{\text{eff}} & 0 & 0 & 0 \\ d_{xz} & \lambda_{\text{eff}} & 0 & 0 & 0 & 0 \\ d_{yz} & 0 & 0 & 0 & -\lambda_{\text{eff}} & -\sqrt{3}\lambda_{\text{eff}} \\ d_{x^2-y^2} & 0 & 0 & \lambda_{\text{eff}} & 0 & 0 \\ d_{z^2} & 0 & 0 & \sqrt{3}\lambda_{\text{eff}} & 0 & 0 \end{array} \quad (\text{C2})$$

		on-site VI_2					Z_1 -bond VI_2				
λ_z		d_{xy}	d_{xz}	d_{yz}	$d_{x^2-y^2}$	d_{z^2}	d_{xy}	d_{xz}	d_{yz}	$d_{x^2-y^2}$	d_{z^2}
d_{xy}		0	0	0	-31	0	0	-1	1	-17	0
d_{xz}		0	0	-38	2	0	1	0	-2	-1	-3
d_{yz}		0	38	0	2	0	-1	2	0	-1	3
$d_{x^2-y^2}$		31	-2	-2	0	-6	17	1	1	0	36
d_{z^2}		0	0	0	6	0	0	3	-3	-36	0
λ_x		d_{xy}	d_{xz}	d_{yz}	$d_{x^2-y^2}$	d_{z^2}	d_{xy}	d_{xz}	d_{yz}	$d_{x^2-y^2}$	d_{z^2}
d_{xy}		0	-38	0	-1	-2	0	-1	-12	1	-1
d_{xz}		38	0	0	0	-2	1	0	0	21	-1
d_{yz}		0	0	0	16	27	12	0	0	0	-2
$d_{x^2-y^2}$		1	0	-16	0	-6	-1	-21	0	0	1
d_{z^2}		2	2	-27	6	0	1	1	2	-1	0
λ_y		d_{xy}	d_{xz}	d_{yz}	$d_{x^2-y^2}$	d_{z^2}	d_{xy}	d_{xz}	d_{yz}	$d_{x^2-y^2}$	d_{z^2}
d_{xy}		0	0	38	-1	2	0	12	1	1	1
d_{xz}		0	0	0	16	-27	-12	0	0	0	2
d_{yz}		-38	0	0	-0	2	-1	0	0	21	1
$d_{x^2-y^2}$		1	-16	0	0	-6	-1	0	-21	0	1
d_{z^2}		-2	27	-2	6	0	-1	-2	-1	-1	0

TABLE VII. Relativistic hopping parameters λ_ν (in meV) for VI_2 on-site and on a Z_1 -bond as defined in Fig. 1, with $\nu \in \{x, y, z\}$ and $\mathcal{H}_{\text{hop}} = t_{ij}^{\alpha\beta} + \frac{i}{2} \vec{\lambda}_{ij}^{\alpha\beta} \cdot \vec{\sigma}$.

$$\begin{array}{c|ccccc} \lambda_y & d_{xy} & d_{xz} & d_{yz} & d_{x^2-y^2} & d_{z^2} \\ \hline d_{xy} & 0 & 0 & \lambda_{\text{eff}} & 0 & 0 \\ d_{xz} & 0 & 0 & 0 & -\lambda_{\text{eff}} & \sqrt{3}\lambda_{\text{eff}} \\ d_{yz} & -\lambda_{\text{eff}} & 0 & 0 & 0 & 0 \\ d_{x^2-y^2} & 0 & \lambda_{\text{eff}} & 0 & 0 & 0 \\ \langle d_{z^2} | & 0 & -\sqrt{3}\lambda_{\text{eff}} & 0 & 0 & 0 \end{array} \quad (\text{C3})$$

As discussed in the main text, comparison to the values obtained for the monolayer structures (see Table VII for the example case VI_2) does not allow to identify one unique effective spin-orbit coupling strength λ_{eff} . This can be attributed to the fact that spin-orbit coupling effects arise mainly from the heavy ligand p elements (here I), not the metal d elements (here V).

On a nearest neighbor bond, one can assume that the crystal-field effects at the ligand site split the p -levels, such that the p_z orbital is split off from the p_x and p_y . This suggests that the z -component of the SOC at the ligand dominates the effect, which couples the p_x and p_y orbitals. In this case, the SOC at the ligand, when projected into the d -orbital Wannier functions, results in a complex hopping $\lambda_{(x^2-y^2; z^2)}^z$. A similar analysis of this situation was done in Ref. 30.

Appendix D: Spin-polarized Wannier function analysis

For completion, we discuss in this section spin-polarized nearest neighbor hopping integrals to give fur-

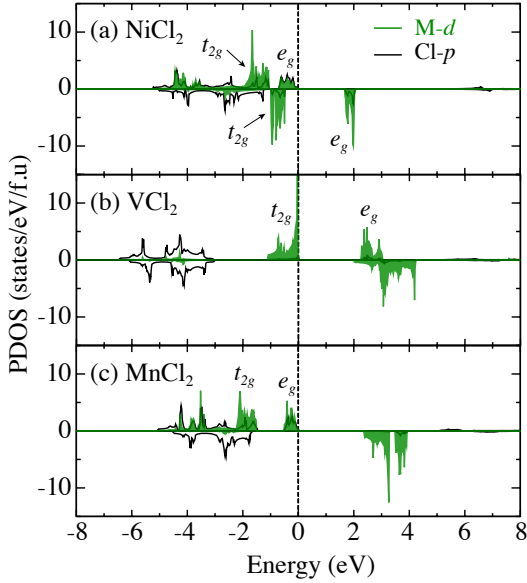


FIG. 4. DOS projected onto $M-d$ and $Cl-p$ orbital states for (a) $NiCl_2$, (b) VCl_2 and (c) $MnCl_2$. Fermi level is set at energy origin.

	$NiCl_2$	VCl_2	$MnCl_2$
t_3	-77	-250	-81
\tilde{t}	37	-33	0.5

TABLE VIII. Hopping integrals t_{eff} (meV) calculated via spin-polarized MLWFs basis set for first nearest neighbor coupling in ferromagnetic spin configuration.

ther insight into the microscopic mechanism behind the magnetic couplings in the cases of monolayer MCl_2 ($M=\{V, Mn, Ni\}$). After a DFT calculation was performed by using the VASP code⁷⁸ and GGA+ U functional with $U = 1.8$ eV and $J_H = 0.8$ eV, the hopping parameter t_{dd}^{eff} between the transition-metal sites was extracted via the Maximally Localized Wannier Functions (MLWFs) as constructed from projection of five transition-metal d states and six ligand p states⁸⁶. The shapes of the d -orbital MLWFs are shown in Fig. 5(a). Note that the $dp-pd$ hybridization process is implicitly included in t_{dd}^{eff} hopping since the Wannier function has delocalized character reflecting the hybridization with the surrounding ligands' p orbital states. The orbital-dependent hopping integrals between the first nearest neighbour M sites were calculated in ferromagnetic spin configuration.

Figure 4 shows the density of states projected onto $M-d$ and $Cl-p$ orbital states. Strong hybridization between $M-d$ and $Cl-p$ orbitals can be seen in the cases of $NiCl_2$ and $MnCl_2$, but not in VCl_2 , resultant from the different d electron filling. The CFS causes large band gap between e_g and t_{2g} orbital states in Ni minority-spin state and V majority-spin state.

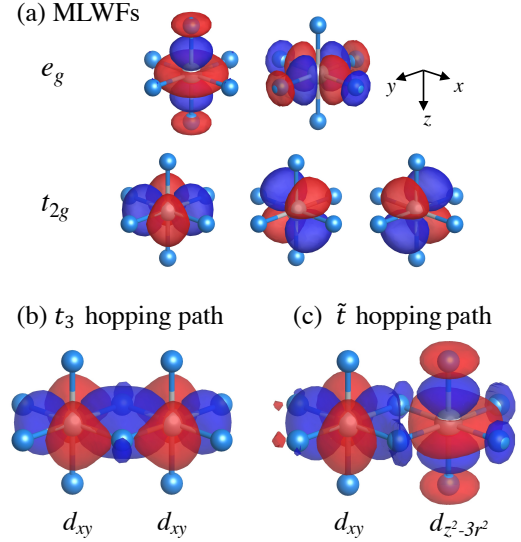


FIG. 5. (a) 3d-orbital MLWFs in VCl_6 octahedral coordination in VCl_2 monolayer. (b, c) Combination of MLWFs for t_3 and \tilde{t} hopping paths in ferromagnetic configuration. Isosurface levels were set at $\pm 0.8 a_0^{-3/2}$. Blue and red colors show opposite signs of MLWF.

As mentioned in Section III B, the nearest neighbor exchange coupling can be explained by the hopping integrals between d_{xy} and d_{xy} orbitals and d_{xy} and d_{z^2} orbitals, namely, t_3 and \tilde{t} . Table VIII lists the calculated hopping parameters through the spin-polarized Wannier functions.

In $NiCl_2$, weak ferromagnetic exchange is attributed to \tilde{t} ($= 37$ meV) hopping between filled t_{2g}^\downarrow state and empty e_g^\uparrow state. Since the t_{2g} state is fully occupied, t_3 hopping does not play any role in the exchange interaction.

In VCl_2 , t_{2g}^\uparrow state is fully occupied while e_g^\uparrow state is empty. It is found that anti-parallel-spin-favored t_3 hopping is much stronger than parallel-spin-favored \tilde{t} hopping. As shown in Fig. 5(b) and (c), t_3 hopping is direct $d-d$ hopping while \tilde{t} hopping is $dp(\sigma)-pd(\pi)$ indirect hopping. This result is consistent with what was discussed in Section III B.

In $MnCl_2$, d^5 electron fully occupies the majority spin state and opens a wide band gap. As being speculated, this leads to weak exchange interaction while $|t_3| \gg |\tilde{t}|$ condition results in anti-parallel spin exchange interaction.

Appendix E: Exchange parameters for alternative U_{avg} and J_{avg} values

To provide context of the dependence on the Coulomb repulsion U_{avg} and Hund's coupling J_{avg} , we list in Table IX the exchange parameters extracted with projED and the 4-states method for $(U_{avg}, J_{avg}) = (1.8, 0.8)$ eV. These parameters were chosen previously by some of the

	projED			4-states		
	NiCl ₂	NiBr ₂	NiI ₂	NiCl ₂	NiBr ₂	NiI ₂
J_1	-2.2	-2.1	-2.5	-5.1	-6.0	-8.0
K_1	0.	+0.1	+1.3	0.	+0.2	+3.2
Γ_1	0.	0.	0.	0.	0.	0.
Γ'_1	0.	0.	-0.1	0.	0.	-0.2
J_2	-0.1	-0.1	-0.1	-0.1	-0.1	-0.3
J_3	+1.2	+1.7	+2.4	+1.7	+2.9	+5.8
A_c	0.	+0.1	+0.7	0.	0.	+0.6

	projED			4-states		
	VCl ₂	VBr ₂	VI ₂	VCl ₂	VBr ₂	VI ₂
J_1	+7.8	+5.0	+2.6	+8.6	+5.1	+1.8
K_1	0.	0.	0.	0.	0.	0.
Γ_1	0.	0.	0.	0.	0.	0.
Γ'_1	0.	0.	0.	0.	0.	0.
J_2	0.	+0.1	+0.1	0.	0.	+0.1
J_3	0.	+0.1	+0.1	-0.1	+0.2	+0.3
A_c	0.	0.	-0.1	0.	0.	0.

	projED			4-states		
	MnCl ₂	MnBr ₂	MnI ₂	MnCl ₂	MnBr ₂	MnI ₂
J_1	+1.2	+1.0	+0.9	+0.4	+0.3	+0.3
K_1	0.	0.	0.	0.	0.	0.
Γ_1	0.	0.	0.	0.	0.	0.
Γ'_1	0.	0.	0.	0.	0.	0.
J_2	0.	0.	+0.1	0.	0.	+0.1
J_3	+0.1	+0.1	+0.1	+0.1	+0.1	+0.1
A_c	0.	0.	0.	0.	0.	0.

TABLE IX. Exchange parameters (in meV) for the MX_2 monolayer structures using $(U_{\text{avg}}, J_{\text{avg}}) = (1.8, 0.8)$ eV; extracted with the projED method (left) and the 4-states energy mapping method (right).

authors^{47,51} for the analysis of the NiX_2 materials.

Not surprisingly, the trends agree with the parameters listed in the main text in Tables II to IV for the values determined with constrained RPA. The overall tendency toward larger absolute values in both methods can be assigned to the smaller Coulomb repulsion, which results in an overall increase of the magnetic exchange.

* These two authors contributed equally

¹ A. P. Ramirez, *Annu. Rev. Mater. Res.* **24**, 453 (1994).

² L. Balents, *Nature* **464**, 199 (2010).

³ C. Lacroix, P. Mendels, and F. Mila (Eds.), *Introduction to Frustrated Magnetism*, Springer Series in Solid-State Sciences, Vol. 164 (Berlin, 2011).

⁴ O. A. Starykh, *Rep. Prog. Phys.* **78**, 052502 (2015).

⁵ W. Liu and Y. Xu (Eds.), *Spintronic 2D Materials: Fundamentals and Applications*, Materials Today (Elsevier Science, 2019).

⁶ A. N. Vasiliev, O. S. Volkova, E. A. Zvereva, and M. M. Markina (Eds.), *Low-Dimensional Magnetism* (CRC Press, 2019).

⁷ S. M. Winter, Y. Li, H. O. Jeschke, and R. Valentí, *Phys. Rev. B* **93**, 214431 (2016).

⁸ S. M. Winter, K. Riedl, P. A. Maksimov, A. L. Chernyshev, A. Honecker, and R. Valentí, *Nat. Commun.* **8**, 1152 (2017).

⁹ H.-S. Kim and H.-Y. Kee, *Phys. Rev. B* **93**, 155143 (2016).

¹⁰ R. Yadav, N. A. Bogdanov, V. M. Katukuri, S. Nishimoto,

J. van den Brink, and L. Hozoi, *Sci. Rep.* **6**, 37925 (2016).

¹¹ Y. S. Hou, H. J. Xiang, and X. G. Gong, *Phys. Rev. B* **96**, 054410 (2017).

¹² C. Eichstaedt, Y. Zhang, P. Laurell, S. Okamoto, A. G. Eguiluz, and T. Berlijn, *Phys. Rev. B* **100**, 075110 (2019).

¹³ P. Laurell and S. Okamoto, *npj Quantum Mater.* **5**, 2 (2020).

¹⁴ J. L. Lado and J. Fernández-Rossier, *2D Mater.* **4**, 035002 (2017).

¹⁵ C. Xu, J. Feng, H. Xiang, and L. Bellaiche, *npj Computational Materials* **4**, 57 (2018).

¹⁶ O. Besbes, S. Nikolaev, N. Meskini, and I. Solovyev, *Phys. Rev. B* **99**, 104432 (2019).

¹⁷ I. Lee, F. G. Utermohlen, D. Weber, K. Hwang, C. Zhang, J. van Tol, J. E. Goldberger, N. Trivedi, and P. C. Hammel, *Phys. Rev. Lett.* **124**, 017201 (2020).

¹⁸ A. Kartsev, M. Augustin, R. F. Evans, K. S. Novoselov, and E. J. G. Santos, *npj Comput. Mater.* **6**, 1 (2020).

¹⁹ Y. O. Kvashnin, A. Bergman, A. I. Lichtenstein, and M. I. Katsnelson, *Phys. Rev. B* **102**, 115162 (2020).

- ²⁰ P. P. Stavropoulos, X. Liu, and H.-Y. Kee, *Phys. Rev. Research* **3**, 013216 (2021).
- ²¹ A. Edström, D. Amoroso, S. Picozzi, P. Barone, and M. Stengel, *Phys. Rev. Lett.* **128**, 177202 (2022).
- ²² Y. Tokunaga, D. Okuyama, T. Kurumaji, T. Arima, H. Nakao, Y. Murakami, Y. Taguchi, and Y. Tokura, *Phys. Rev. B* **84**, 060406 (2011).
- ²³ T. Kurumaji, S. Seki, S. Ishiwata, H. Murakawa, Y. Kaneko, and Y. Tokura, *Phys. Rev. B* **87**, 014429 (2013).
- ²⁴ T. Kurumaji, S. Seki, S. Ishiwata, H. Murakawa, Y. Tokunaga, Y. Kaneko, and Y. Tokura, *Phys. Rev. Lett.* **106**, 167206 (2011).
- ²⁵ Y. Li, D. Chen, X. Dong, L. Qiao, Y. He, X. Xiong, J. Li, X. Peng, J. Zheng, X. Wang, *et al.*, *J. Phys. Condens. Matter* **32**, 335803 (2020).
- ²⁶ Q. Song, C. A. Occhialini, E. Ergeçen, B. Ilyas, D. Amoroso, P. Barone, J. Kapeghian, K. Watanabe, Taniguchi, Takashi, A. S. Botana, S. Picozzi, N. Gedik, and R. Comin, *Nature* **602**, 601–605 (2022).
- ²⁷ A. O. Fumega and J. L. Lado, *2D Mater.* **9**, 025010 (2022).
- ²⁸ Z. Jiang, Y. Li, W. Duan, and S. Zhang, *Phys. Rev. Lett.* **122**, 236402 (2019).
- ²⁹ A. S. Botana and M. R. Norman, *Phys. Rev. Materials* **3**, 044001 (2019).
- ³⁰ P. P. Stavropoulos, D. Pereira, and H.-Y. Kee, *Phys. Rev. Lett.* **123**, 037203 (2019).
- ³¹ K. Riedl, Y. Li, R. Valentí, and S. M. Winter, *Phys. Status Solidi B* **256**, 1800684 (2019).
- ³² H. Xiang, C. Lee, H.-J. Koo, X. Gong, and M.-H. Whangbo, *Dalton Trans.* **42**, 823 (2013).
- ³³ X. Li, H. Yu, F. Lou, J. Feng, M.-H. Whangbo, and H. Xiang, *Molecules* **26**, 803 (2021).
- ³⁴ P. W. Anderson, *Phys. Rev.* **79**, 350 (1950).
- ³⁵ J. Kanamori, *J. Phys. Chem. Solids* **10**, 87 (1959).
- ³⁶ A. Kitaev, *Ann. Phys.* **321**, 2 (2006).
- ³⁷ S. M. Winter, A. A. Tsirlin, M. Daghofer, J. van den Brink, Y. Singh, P. Gegenwart, and R. Valentí, *J. Phys. Condens. Matter* **29**, 493002 (2017).
- ³⁸ J. P. Perdew, K. Burke, and M. Ernzerhof, *Phys. Rev. Lett.* **77**, 3865 (1996).
- ³⁹ F. Aryasetiawan, M. Imada, A. Georges, G. Kotliar, S. Biermann, and A. I. Lichtenstein, *Phys. Rev. B* **70**, 195104 (2004).
- ⁴⁰ F. Aryasetiawan, K. Karlsson, O. Jepsen, and U. Schönberger, *Phys. Rev. B* **74**, 125106 (2006).
- ⁴¹ E. Pavarini, E. Koch, F. Anders, and M. Jarrell (Eds.), *Correlated Electrons: From Models to Materials*, Schriften des Forschungszentrums Jülich: Modeling and Simulation, Vol. 2 (Jülich, 2012).
- ⁴² H. Eschrig and K. Koepnik, *Phys. Rev. B* **80**, 104503 (2009).
- ⁴³ K. Koepnik and H. Eschrig, *Phys. Rev. B* **59**, 1743 (1999).
- ⁴⁴ A. Georges, L. d. Medici, and J. Mravlje, *Annu. Rev. Condens. Matter Phys.* **4**, 137 (2013).
- ⁴⁵ A. Abragam and B. Bleaney, *Electron paramagnetic resonance of transition ions* (OUP Oxford, 2012).
- ⁴⁶ S. M. Winter, arXiv preprint arXiv:2204.09856 (2022).
- ⁴⁷ D. Amoroso, P. Barone, and S. Picozzi, *Nat. Commun.* **11**, 5784 (2020).
- ⁴⁸ P. A. Lindgard, R. J. Birgeneau, H. J. Guggenheim, and J. Als-Nielsen, *J. Phys. C: Solid State Phys.* **8**, 1059 (1975).
- ⁴⁹ P. Day, A. Dinsdale, E. R. Krausz, and D. J. Robbins, *J. Phys. C: Solid State Phys.* **9**, 2481 (1976).
- ⁵⁰ J. Y. Ni, X. Y. Li, D. Amoroso, X. He, J. S. Feng, E. J. Kan, S. Picozzi, and H. J. Xiang, *Phys. Rev. Lett.* **127**, 247204 (2021).
- ⁵¹ D. Amoroso, P. Barone, and S. Picozzi, *Nanomaterials* **11**, 1873 (2021).
- ⁵² K. Katsumata and K. Yamasaka, *J. Phys. Soc. Jpn.* **34**, 346 (1973).
- ⁵³ D. Billerey, C. Terrier, A. J. Pointon, and J. P. Redoules, *J. Magn. Magn. Mater.* **21**, 187 (1980).
- ⁵⁴ C. Xu, J. Feng, M. Kawamura, Y. Yamaji, Y. Nahas, S. Prokhorenko, Y. Qi, H. Xiang, and L. Bellaiche, *Phys. Rev. Lett.* **124**, 087205 (2020).
- ⁵⁵ L. Régnault, J. Rossat-Mignod, A. Adam, D. Billerey, and C. Terrier, *J. physique* **43**, 1283 (1982).
- ⁵⁶ E. Rastelli, A. Tassi, and L. Reatto, *Physica B+C* **97**, 1 (1979).
- ⁵⁷ K. Katsumata and M. Date, *J. Phys. Soc. Jpn.* **27**, 1360 (1969).
- ⁵⁸ S. Babu, K. Prokeš, Y. K. Huang, F. Radu, and S. K. Mishra, *J. Appl. Phys.* **125**, 093902 (2019).
- ⁵⁹ D. Billerey, C. Terrier, N. Ciret, and J. Kleinclauss, *Phys. Lett. A* **61**, 138 (1977).
- ⁶⁰ D. Billerey, C. Terrier, R. Mainard, and A. J. Pointon, *Phys. Lett. A* **77**, 59 (1980).
- ⁶¹ S. R. Kuindersma, J. P. Sanchez, and C. Haas, *Physica B+C* **111**, 231 (1981).
- ⁶² P. Day and K. R. A. Ziebeck, *J. Phys. C: Solid State Phys.* **13**, L523 (1980).
- ⁶³ A. Adam, D. Billerey, C. Terrier, R. Mainard, L. P. Regnault, J. Rossat-Mignod, and P. Mériel, *Solid State Commun.* **35**, 1 (1980).
- ⁶⁴ P. Day, M. W. Moore, T. E. Wood, D. M. Paul, K. R. Ziebeck, L. P. Regnault, and J. Rossat-Mignod, *Solid State Commun.* **51**, 627 (1984).
- ⁶⁵ K. Riedl, E. Gati, D. Zielke, S. Hartmann, O. M. Vyaselev, N. D. Kushch, H. O. Jeschke, M. Lang, R. Valentí, M. V. Kartsovnik, and S. M. Winter, *Phys. Rev. Lett.* **127**, 147204 (2021).
- ⁶⁶ M. Niel, C. Cros, G. Le Flem, M. Pouchard, and P. Hagenmuller, *Physica B+C* **86**, 702 (1977).
- ⁶⁷ H. Kadowaki, K. Ubukoshi, K. Hirakawa, J. L. Martínez, and G. Shirane, *J. Phys. Soc. Jpn.* **56**, 4027 (1987).
- ⁶⁸ H. Kadowaki, K. Ubukoshi, and K. Hirakawa, *J. Phys. Soc. Jpn.* **54**, 363 (1985).
- ⁶⁹ K. Hirakawa, H. Kadowaki, and K. Ubukoshi, *J. Phys. Soc. Jpn.* **52**, 1814 (1983).
- ⁷⁰ M. Nishi, Y. Ito, H. Kadowaki, and K. Hirakawa, *J. Phys. Soc. Jpn.* **53**, 1214 (1984).
- ⁷¹ S. Kuindersma, C. Haas, J. Sanchez, and R. Al, *Solid State Commun.* **30**, 403 (1979).
- ⁷² *Physics division semiannual progress report for period ending September 10, 1957*, Tech. Rep. (Oak Ridge National Lab., Tenn., 1958).
- ⁷³ T. Sato, H. Kadowaki, and K. Iio, *Physica B: Condens. Matter* **213**, 224 (1995).
- ⁷⁴ K. Iio, H. Masuda, H. Tanaka, and K. Nagata, *J. Magn. Magn. Mater.* **90**, 265 (1990).
- ⁷⁵ T. Sato and H. Kadowaki, *Neutron scattering study of MnX₂ (X= Br, I)*, Tech. Rep. (1993).
- ⁷⁶ J. Cable, M. Wilkinson, E. Wollan, and W. Koehler, *Phys. Rev.* **125**, 1860 (1962).
- ⁷⁷ O. I. Utesov and A. V. Syromyatnikov, *Phys. Rev. B* **95**, 214420 (2017).

- ⁷⁸ G. Kresse and J. Furthmüller, *Phys. Rev. B* **54**, 11169 (1996).
- ⁷⁹ M. A. McGuire, *Crystals* **7**, 121 (2017).
- ⁸⁰ H. Jiang, R. I. Gómez-Abal, X. Li, C. Meisenbichler, C. Ambrosch-Draxl, and M. Scheffler, *Computer Phys. Commun.* **184**, 348 (2012).
- ⁸¹ Y. Yekta, H. Hadipour, E. Şaşıoğlu, C. Friedrich, S. A. Jafari, S. Blügel, and I. Mertig, *Phys. Rev. Materials* **5**, 034001 (2021).
- ⁸² A. I. Liechtenstein, V. I. Anisimov, and J. Zaanen, *Phys. Rev. B* **52**, R5467 (1995).
- ⁸³ H. Liu and G. Khaliullin, *Phys. Rev. B* **97**, 014407 (2018).
- ⁸⁴ S. M. Winter, K. Riedl, and R. Valentí, *Phys. Rev. B* **95**, 060404 (2017).
- ⁸⁵ J. G. Rau, E. K.-H. Lee, and H.-Y. Kee, *Phys. Rev. Lett.* **112**, 077204 (2014).
- ⁸⁶ T. P. T. Nguyen, K. Yamauchi, T. Oguchi, D. Amoroso, and S. Picozzi, *Phys. Rev. B* **104**, 014414 (2021).